The impact of a passive tuned mass damper on offshore single-blade installation

Zhiyu Jiang[a,b,*]

[a]*Department of Marine Technology, Norwegian University of Science and Technology (NTNU), NO-7491 Trondheim, Norway*
[b]*Centre for Research-based Innovation of Marine Operations (SFI MOVE), NTNU, NO-7491 Trondheim, Norway*

Abstract

Single-blade installation is a method suitable for the installation of blades on large wind turbines. For single-blade installations on offshore monopile-type wind turbines, a jack-up vessel is often involved, and each blade is mated with the hub at the tower top. Prior to the alignment phase, the blade root and the nacelle at the tower top experience relative motions. The blade-root motions are induced by the wind loads, and the nacelle motions are due to the resonant vibrations of the monopile support structure under wave loading. To alleviate the relative motions and to facilitate the alignment process, external passive tuned mass dampers can be installed on the monopile support structures. This work investigates the application potential of tuned mass dampers in single-blade installation. Multibody simulations were conducted under collinear wind and waves conditions, and the relative motions between the blade-root and the hub were analysed. It was found that when an optimally tuned passive damper is considered for the monopile structure, the reduction in the critical motion radius can reach up to 30%.

Keywords: single-blade installation; tuned mass damper; monopile vibration; hub motion; wind and waves; outcrossing

*Corresponding author
Email address: zhiyu.jiang1896@gmail.com (Zhiyu Jiang)

1. Introduction

Monopile support structures remain the most popular substructure type in the European offshore wind industry, representing 88% of all installed foundations in 2016 [1]. This type of support structure has a single column and is relatively cost effective for shallow water depths less than 40 meters (m). With the largest announced monopile diameter approaching 8 m [2], the major concern with monopile support structures relates to their sensitivity to wave loading [3]. The dimensioning of these structures is often driven by fatigue loads. When designing the eigen frequencies of the tower, a common practice is to avoid coincidence with the fundamental frequencies (1P) and the blade passing frequencies of a 3-bladed rotor (3P) [4]. Still, along with the growing sizes of wind turbines, the first eigen frequencies of the fore-aft and side-side modes may approach the upper limit of wave frequencies (0.25 Hz) and cause greater resonant responses of the support structures.

Installations of monopile-type wind turbines often involve a heavy lift vessel. Upon arrival on site, the pile is upended and driven into the seabed by a hydraulic hammer, and the transition piece is grouted onto the pile. Then, the wind turbine components, including the tower, nacelle, hub, and blades, are to be installed. A number of options exist for turbine installation with varying numbers of pre-assembled components [5, 6]. Among the options, there is a method that involves one lift for the tower, one lift for the nacelle and hub, and separate lifts for each blade. This method allows for a more efficient use of deck space but may be susceptible to delays because of high winds. Single-blade installation refers to the method of blade installation and was reported to be convenient up to wind speed from 8–12 m/s [7]. Fig. 1 illustrates typical scenarios of single-blade installation for offshore monopile-type wind turbines. To improve this performance, efforts have been made to better understand the blade aerodynamics during installation [7, 8, 9, 10, 11], and to develop numerical simulation tools [12]. Specialised installation equipment [13, 14] has also been created to cater to the market need. For example, the Boom Lock technology [14] enables to mitigate the blade motions by locking the crane hook during the lifting process. These mitigation measures focused on the blade responses. On the other hand, according to industrial experiences [15], monopile vibrations are another source that contribute to delays during single-blade installations. In a recent work [16], it was shown that in the final blade installation stage, the hub motions at the tower top can be more important than the blade responses given the presence of significant resonant responses of the monopile.

Damping is critical insofar as structural resonant responses are concerned. For an offshore monopile structure without external dampers, the total damping consists of structural damping, soil damping, hydrodynamic damping, and aerodynamic damping. The overall damping ratio of the first fore-aft mode is approximately 1% [17, 18]. During wind turbine installation, there is even less damping on the monopile structure because of the lack of aerodynamic damping from the rotating blades. Thus, supplemental dampers can offer potential solutions for the structural control of monopiles during single-blade installations. There are passive, active, and semiactive damping strategies [19]. Passive systems are simple in form and require no external energy input. Mass-spring-damper systems with constant parameters are such examples. It is necessary to tune the system parameters to absorb energy at one of the natural frequencies of the structure. In contrast, active systems are complex and require control systems with force actuators. These systems have greater load reduction potential at the expense of larger power consumption [20]. Semiactive systems offer the reliability of passive devices while maintain the versatility and adaptability of fully active systems [19]. In some cases, feedback control is used by semiactive systems to tune the system parameters in response to the structural motions, and the system can operate on battery power. There is a wide range of damping devices, such as tuned mass dampers (TMDs), tuned liquid column dampers [21, 22], viscous fluid dampers [23], and magnetorheological dampers [24]. Early applications are found in civil engineering structures, including buildings and bridges [19, 25]. Among the various forms of dampers, TMDs have been recently considered for offshore bottom-fixed and floating wind turbines [20, 26, 27, 28, 29, 30]. Lackner and Rotea [20] demonstrated that TMDs can improve the structural responses of barge- and monopile-type offshore wind turbines, targeting the dominant fore-aft mode for monopile-type wind turbines and the platform-pitch mode for barge-type wind turbines, respectively. In another work, Lackner and Rotea [26] considered the active control approach and showed a beneficial effect on fatigue load reduction of a barge-type floating wind turbine. Si et al. [29] applied a passive TMD for a spar-type floating wind turbine and found that the TMD is most effective when the spar platform is working at above-rated wind speeds in resonant motion. Stewart and Lackner [28] studied a monopile-type wind turbine and reported the effects of TMDs on reducing the tower base moment, especially in the side-to-side direction. These studies addressed the effect of TMDs on wind turbine performance under operational and parked conditions.

To the author's knowledge, no publication is found regarding application of TMDs in scenarios

of offshore single-blade installations. Motivated by the application potential of TMDs and the challenges faced during single-blade installation, this work will investigate the influence of a passive TMD on the final blade installation stage. The outcome of this paper may be used to facilitate the application of TMDs during offshore wind turbine installations, and to reduce the cost of energy of offshore wind turbines. The remainder of this paper will be organised as follows. Section 2 defines the research problem and presents the analysis procedure. Section 3 introduces the developed numerical tools and the modelling approach. Section 5 describes the representative monopile system and the single-blade system. Section 6 specifies the load cases for the numerical simulations. Section 7 presents a comparison of the simulation results with and without TMD. Finally, Section 8 concludes the paper.

2. PROBLEM STATEMENT

Single-blade installations are often performed under the assistance of a jack-up installation vessel. Before the blade installation starts, the jack-up vessel is elevated well above the wave zone, providing a stable base for the lifting operation. During the installation, each blade is lifted by the crane to the hub height and attached to the hub individually. Fig. 2(a) illustrates a scenario of the blade final installation stage. The origin of the global coordinate system is placed on the monopile structure at the mudline level. Unless otherwise specified, the global coordinate system is referred to in the following. As the blade root approaches the hub, the wind-induced blade-root oscillations are primarily in the yz-plane, and the tugger lines constrain the blade motions. The blade root and the hub make an alignment pair. Located at the tower top, the hub also experiences fore-aft motions in the yz-plane, especially when the waves are collinear with the wind. At this stage, the relative motions between the blade root and the hub can be reliably measured by the onboard monitoring system such as the Differential Global Positioning System (DGPS) and the Real-Time Kinematic (RTK) satellite navigation technology [31].

Often, the blade root and the hub are not perfectly aligned (Fig. 2(b)). η_r is defined as the relative motion radius. This value is the distance between the centres of the blade and hub and varies with time. In practice, there is a circular safety boundary with a radius of R_{sb}. If $\eta_r < R_{sb}$, the centre axes can be manually aligned. Otherwise, a time delay may be expected for the alignment operation. Fig. 2 sketches the outcrossing process of η_r over the safety boundary. The starting point of η_r is within the safety boundary, and it outcrosses the boundary twice along the black

track. For any specified time interval, the outcrossing number can be counted, and the outcrossing rate refers to the frequency of outcrossings. The lower the outcrossing rate, the higher success rate of alignment. The outcrossing rate, ν, is a function of η_r. Herein, the critical outcrossing rate, ν_{cr}, is defined as the allowable outcrossing rate for a specified R_{sb}. ν_{cr} is often empirically selected based on knowledge of the installation facilities. In this paper, it is assumed that the final installation stage lasts a maximum of 30 minutes and that a successful alignment requires less than 10 outcrossings out of the safety boundary during this time interval (ν_{cr}=$5.5 \cdot 10^{-3}$ Hz). These representative values were selected after discussion with a consultant experienced with single-blade installations [15].

Fig. 3 presents the analysis procedure of this work. First, the monopile system and the single blade system are numerically modelled. The monopile structure is modelled with or without the TMD. Second, time-domain simulations are conducted under wind and wave conditions. From the simulations, the blade-root and hub motions can be obtained, and time histories of the relative motions radius in the yz-plane are calculated. From level crossing analysis, the relation between η_r and ν_r is established, and η_{rcr} can be obtained for the given ν_{cr}. The response surface methodology is applied during the comparison of results.

3. SIMULATION TOOLS

In this research, the dynamic responses of a monopile system and a single blade system are simultaneously simulated in HAWC2. A brief description of the features of the simulation tools follows.

3.1. HAWC2-TMD

HAWC2 is an aeroelastic code developed by Technical University of Denmark Wind Energy and is intended for realistic simulations of wind turbine response in the time domain. HAWC2 consists of models describing external effects, applied loads, structural dynamics, and the connection to control system.

A schematic of the TMD position is shown in Fig. 4. The TMD is assumed to be installed inside the tower wall at the tower top, and it can be useful during installations of both the nacelle and blades. The implementation of an additional TMD system within HAWC2 is achieved by using an external dynamic link library (DLL). The DLL feature provides a generalised interface, allowing for modelling external loading or controlled actions; see [32, 33, 34]. Fig. 5 shows the

procedure for modelling a TMD in HAWC2. After developing the "TMD.DLL", it is necessary to specify the node to which the TMD is connected in the HAWC2 input file (*.*htc*). A separate data file including the TMD parameters will be needed, too. The calculation procedure during the time-domain simulations is illustrated in Fig. 6. The present TMD module was developed by the author with reference to the ServoDyn module of FAST v8 [35]. A one degree-of-freedom (DOF) element is implemented, acting in the fore-aft (y) direction. Both the global inertial reference frame and the non-inertial reference frame fixed to the neutral position of the TMD are used. At each time step, the HAWC2 core outputs the position of the tower top as well as the linear and angular velocities and accelerations in the global frame. Those data are transformed to calculate the TMD states in the non-inertial frame. After updating the nonlinear first-order state-space equations given by Eq. (A.14), new TMD states are obtained, and the reaction forces and moments acting on the tower top are fed back into HAWC2. Detailed theories of a 1-DOF TMD can be found in Appendix A. The properties of the TMD, such as mass (M_y), damping (C_y), stiffness (K_y) and initial positions (P_x, P_y, P_z), are read during the initialisation of the DLL.

3.2. Structural Model

The structural formulation of HAWC2 is based on multibody dynamics [36]. The multibody formulation provides flexibility in the modelling of offshore wind turbines and guyed support structures. In the structural model, the structure is divided into a number of independent coupled bodies. Large translations and rotations are allowed at the coupling joint, and small deflections are assumed within each body.

3.3. Aerodynamic Model

For rotating blades, the aerodynamic model in HAWC2 is based on the blade element momentum theory, which is modified to handle unsteady aeroelastic features, such as dynamic inflow and dynamic stall [37].

For single-blade installation scenarios, the blade is hindered from rotating, and the steady aerodynamic lift and drag coefficients are used to determine the wind loads on each blade section. The cross-flow principle [38] is applied during the load calculation, so the wind components in the spanwise direction are ignored. This approach is generally applicable to situations without yaw but may require corrections for yawed flow [10].

3.4. Hydrodynamic Model

Morison's formula is used to calculate the hydrodynamic loads on a slender structure. For a monopile support structure, the length is discretised into a few strips, and the hydrodynamic force per unit length normal to each strip can be expressed as

$$f_s = \rho C_M \frac{\pi D^2}{4} \ddot{x_w} - \rho(C_M - 1)\frac{\pi D^2}{4}\ddot{\eta}_1 + \frac{1}{2}\rho C_D D(\dot{x}_w - \dot{\eta}_1)|\dot{x}_w - \dot{\eta}_1| \tag{1}$$

where C_M and C_D denote the mass and drag coefficients, respectively. $\dot{x}_w$ and $\ddot{x}_w$ stand for the water particle velocity and acceleration, respectively, at the strip centre. $\dot{\eta}_1$ and $\ddot{\eta}_1$ are the cylinder's velocity and acceleration. In Eq. (1), the first term includes the Froude-Kriloff (FK) and diffraction force, the second term is the inertial force, and the last term is the quadratic drag force [39]. Note that the wave forces are estimated using the undisturbed velocity distribution of the incident waves, and the wavelength is assumed to be large relative to the diameter. For offshore monopile support structures with characteristic diameters of 3 to 5 m, the total hydrodynamic force is dominated by the inertial part [3].

3.5. Soil Model

For an offshore monopile structure, there is a pile penetration below the seabed, and the pile foundation uses lateral loading of the soil to counteract the loads from the supported structure. In HAWC2, the spring stiffness in the axial, lateral, and rotational directions can be input along the specified portion of the pile to model the soil. In addition, a Rayleigh damping factor can be used to tune the soil damping [36].

4. Response Surface Methodology

Response surface methodology, or RSM, is a collection of mathematical and statistical techniques for the modelling and analysis of problems in which a response of interest is affected by severable variables [40]. RSM is often considered an effective method for creating a surrogate model representing the difficult analytical expression of physical quantities. For example, suppose f is a function of the levels of two variables, x_1 and x_2

$$f = g(x_1, x_2) + \epsilon \tag{2}$$

where ϵ can be representative of the noise in the response f. If the expected response is denoted by $E(f) = g(x1, x2) = \hat{f}$, then the surface represented by

$$\hat{f} = g(x_1, x_2) \tag{3}$$

is called a response surface (RS). The RS is often represented graphically; see Fig. 7 for an example.

Because the relation between the response and the independent variables is usually unknown, the first step in RSM is to find an approximation for the true functional relation between f and the independent variables. The first-order model using linear polynomial can be the simplest form of RS

$$f = \lambda_0 + \lambda_1 x_1 + \lambda_2 x_2 + \cdots + \lambda_k x_k + \epsilon \tag{4}$$

If there is curvature in the system, then a polynomial of higher degree can be used, such as the second-order model

$$f = \lambda_0 + \sum_{i=1}^{k} \lambda_i x_i + \sum_{i=1}^{k} \lambda_{ii} x_i^2 + \sum \sum_{i<j} \lambda_{ij} x_i x_j + \epsilon \tag{5}$$

In cases of more complex relations, high-order polynomials, or other metamodel techniques may be considered including the artificial neural network [41], the radial basis functions [42], and the Kirging methods [43].

In Section 6, both low- and high-order polynomials were selected to represent the relation between the motion response and environmental variables.

5. SYSTEM DESCRIPTION

The single-blade installation system includes two independent sub-systems. The first sub-system consists of a monopile support structure, a tower structure, a nacelle, and three hubs (Fig. 8(a)). The second sub-system is composed of a blade, three lift wires, and two tugger lines (Fig. 8(b)). These sub-systems will be described in the following.

5.1. Assembled Monopile System

The first sub-system is a modification of the Phase II model of the Offshore Code Comparison Collaboration (OC3) Project. The Phase II model considers the NREL 5 MW wind turbine, tower, and monopile with a flexible foundation, and selected structural properties are presented in Table 1. Note that for the three-bladed wind turbine, installation of the first blade is considered here. For installation of the second and the third blade, the total stiffness of the assembled system reduces, and f_{n1} decreases from 0.26 Hz to 0.25 Hz. Consequently, dynamic response of the monopile will slightly increase for wave periods above 4 s. The numerical model is available from *www.hawc2.dk*. The distributed springs model is used for the pile foundation. This model idealises the monopile

with flexible foundation as a free-free beam with lateral (Winkler-type) springs distributed along the subsoil portion of the monopile [44]. The spring stiffness constants of the subsoil portion are depth dependent and are calculated based on the linearisation of the p-y curves [45].

The original Phase II model considers a fully assembled wind turbine with the blades attached to the hubs. To represent a more realistic scenario, the blades from the structural model (Fig. 8(a)), and the soil damping factor was calibrated such that the total damping ratio (ζ_t) equals 1%. Among ζ_t, structural damping contributes to fifteen percent ($\zeta_{struct} = 0.15\%$), and the remaining amount comes from soil damping ($\zeta_{soil} = 0.85\%$). Calibrating the soil damping factor is a simplified way for obtaining a realistic total damping ratio [30], which is important to structural responses. The obtained total damping ratio is aligned with the experimentally estimated values reported in [4, 17].

Only one TMD in the y-direction is considered, and the properties of the optimised TMD are summarised in Table 2. To select the parameters of the TMD, the mass of the TMD (M_y) was first determined empirically and the value of k_y was calculated such that the natural frequency of TMD (f_y) is identical to the first fore-aft mode of the tower. Then, a series of decay tests of the assembled monopile system were conducted without environmental loads. The damping ratio (ζ_y) was selected by minimising the standard deviation of the tower-top displacement. In each numerical decay test, the simulation lasted 200 seconds (s), and a constant force was applied on the tower top during the first 50 s. Fig. 9(a) compares the free vibration part of the test with and without the optimised TMD, and the damping ratio can be calculated accordingly. Compared to the baseline system without a TMD, the optimised TMD enhances ζ_t to approximately 3.94%, and the tower top displays very limited y-displacement after 50 s of free vibration. As shown in Fig. 9(b), the TMD oscillates cyclically about its neutral position and quickly reaches balance, with the maximum displacement exceeding 0.4 m.

5.2. Single-blade System

The second sub-system consists of a blade, three lift wires, and two tugger lines. This model is a simplification of the actual system, which may include a hook, yoke, and other additional elements. In the present model, the upper end of lift wire 1 is connected to the crane tip, and one of the ends of both tugger lines 1 and 2 is connected to the crane boom. These connections are regarded as rigid. Prior to blade installation, the main direction of the wind is measured and known (along the Y_g-axis in Fig. 8(b)), and two tugger lines in the opposite direction are used to counteract the wind-induced forces and moments on the blade and to stabilise the blade motion.

Table 1: Structural properties of the OC3 monopile-tower-nacelle assembly

Description	Symbol	Value[1]
Tower base diameter (m)	D_b	6
Tower top diameter (m)	D_t	3.87
Tower length (m)	H_t	77.6
Monopile length (m)	H_m	66
Pile penetration of monopile (m)	H_p	36
Tower mass (tons)	M_t	237.1
Monopile mass (tons)	M_m	628.1
Nacelle and hub mass (tons)	M_n	296.8
Total mass without blades (tons)	M_{tot}	1162
Natural frequency of the 1st fore-aft mode (Hz)	f_{n1}	0.26

[1] Estimated based on the HAWC2 model

Table 2: Parameters of the tuned mass damper

M_y (kg)	K_y (N/m)	C_y (Ns/m)	ζ_y (%)
20000	53375	5228	8

Wire ropes are commonly used for tugger lines. In the numerical model, each tugger line consists of short segments connected by spherical joints. This feature allows for relative rotation between connecting segments. Thus, the tugger lines are noncompressive. Notice the presence of yokes in Fig. 1. The effect of the yoke is represented using a concentrated mass at the blade's centre of gravity (COG).

Table 3: Main properties of the single-blade installation system

Parameter	*Symbol*	*Value*
Blade mass (tons)	M_{bd}	17.3
Blade length (m)	L_{bd}	61.5
Blade root diameter (m)	D_{bd}	3.54
Yoke weight (ton)	W_{yk}	20
Position of the blade COG from root (m)	Xb_{COG}	20.57
Length of lift wire 1 (m)	L_{l1}	10
Length of lift wire 2 & 3 (m)	L_{l2}	9
Tugger line length (m)	L_t	10
Tugger line unit weight (kg/m)	W_{tl}	306
1st rotational mode about the y-axis (Hz)	f_{r1}	0.04
1st translational mode in the y-direction (Hz)	f_{t1}	0.11

6. LOAD CASES

The "North Sea Center" site is selected as a representative site for wind farms [46]. This site has an average water depth of 29 m, which is close to that of the European offshore wind farms constructed in 2016 [1]. In this study, a water depth of 30 m is considered for the monopile structure.

To have an overview of the long-term wind and wave condition of the site, Fig. 10(a) shows the probability distribution of the mean wind speed based on the 10-year hindcast data, and 90% of the wind speeds are concentrated in the region below 12 m/s. Fig. 10(b) presents the average spectral peak period (T_p) for different combinations of wind speed (U_w) and significant wave height (H_s). For typical operational sea states ($H_s \leq 2$ m), relatively low T_p (≤ 6 s) values are often observed.

Table 4 lists the wind and waves conditions used in the numerical simulations. Here, EC denotes environmental condition, U_{hub} refers to the mean wind speed at hub height, and U_w refers to the mean wind speed at the reference height of 10 m, which is calculated using a wind shear exponent of 0.1 [46]. TI stands for turbulence intensity and is calculated according to IEC wind turbine class III [47]. $EC1$ and $EC2$ correspond to the two representative wind speeds, and approximately 25% and 76% wind speeds at the site are below a U_{hub} of 6 m/s and 12 m/s, respectively. For each U_{hub}, a number of combinations of H_s and T_p are considered, covering a wide range of conditions in offshore installations.

Table 4: Collinear wind-wave conditions considered in the study

EC	U_{hub} [m/s]	U_w [m/s]	TI	H_s [m]	T_p [s]
1	6	4.89	0.20	1.0, 1.5, ...,3.0	4, 6,...,12
2	12	9.78	0.15	1.0, 1.5, ...,3.0	4, 6,...,12

Only the collinear environmental conditions are considered, and both wind and waves propagate in the y-direction. If the wave propagates at a misaligned direction, the condition for the blade alignment is expected to be less critical as the relative motion reduces between the blade root and hub. Irregular waves were generated using the JONSWAP spectrum [48]. For each combination of wind and waves with or without the TMD, six 2400-s simulations with random seed numbers were conducted in the time domain using a time step of 0.01 s. The first 600 s of each simulation were discarded in post-processing to remove start-up transients.

7. RESULTS

The response time series, spectra, and statistics will be presented. To reduce statistical uncertainties, the response statistics are obtained based on an average of the six simulations.

7.1. Hub motions

The hub is located at the top of the tower structure, and its motions are governed by the wave loads on the monopile structure. The standard deviation (STD) of the hub motions in Table 5 can be used to indicate the effectiveness of the TMD under the five investigated T_p values. Here, the subscript "0" refers to the monopile system without a TMD, whereas the subscript "1" refers to the system with a TMD. For either STD_0 or STD_1, the absolute value decreases with increased

T_p because the STD is due to the resonant response of the monopile structure. When T_p is low, irregular waves generated from the wave spectrum have more frequency components near the first fore-aft mode (f_{n1}=0.26 Hz), and greater resonant responses occur. The last column in Table 5 summarises the relative reduction in STD. Overall, the reduction in STD because of the TMD is substantial , especially at lower T_p values.

Table 5: Comparison of the standard deviation of the hub y-displacement, H_s=2.5 m

T_p (s)	STD_0 (m)	STD_1 (m)	(STD_1-STD_0)/STD_0 (%)
4	0.92	0.40	-56.4
6	0.33	0.17	-48.0
8	0.28	0.15	-48.3
10	0.18	0.10	-45.9
12	0.13	0.07	-45.1

Fig. 11(a) shows the time histories of the hub displacement in 600 s under H_s=2.5 m and T_p=6 s. For the monopile system without the TMD, the peak response in the time series exceeds 1 m at approximately t=450 s. In this case, the use of the TMD lowers the peak value to approximately 0.5 m. Fig. 11(b) illustrates the effect in the spectrum. In the figure, two peaks can be identified corresponding to the wave period and the fore-aft mode, respectively. However, the TMD only reduces the peak of f_{n1}. The hub motion radius, η_h, measures the distance between the hub centre and its neutral position. In this section, the blade motion is ignored, and η_h= η_r. As the wave direction is parallel to the y-axis, η_h is dominated by the y-displacement. Hence, a close correlation between Figs. 11(a) and 11(c) is found. For any level of the hub motion radius for a time interval in Fig. 11(c), the outcrossing rate can be obtained, and the relation between η_h and ν is shown in Fig. 11(d). In both curves, ν decreases monotonically as η_h increases. For the given ν_{cr}, the reduction in η_{hcr} exceeds 50% when a TMD is used.

η_{hcr} varies with H_s and T_p. To find an analytical expression for the relation, η_{hcr} is set as the objective function, and H_s and T_p are the two input variables. Then, η_{hcr} can be approximated by a number of basic functions as

$$\hat{f}(X) = \eta_{hcr}(H_s, T_p) = \sum_{k=1}^{m} \lambda_k \delta_k(H_s, T_p) \tag{6}$$

where m is the number of basic functions and λ_k is the unknown coefficient corresponding to the kth basic function δ_k. A second norm of the error between the objective f and response function

$\hat{f}$ can be expressed as

$$Er(\Lambda) = \varepsilon^T \varepsilon = (f - \Delta\Lambda)^T (f - \Delta\Lambda) \tag{7}$$

where the objective vector $f = (f^{(1)}, f^{(2)}, ..., f^{(s)})^T$ is obtained from the simulations at the design points, the coefficient vector $\Lambda = (\lambda_1, ..., \lambda_m)$, and $\Delta\Lambda$ corresponds to the RS estimates at those points. Δ is the matrix of the basic functions evaluated at the s sampling points, which is

$$\Delta = \begin{bmatrix} \delta_1(X^1) & \cdots & \delta_M(X^1) \\ \vdots & \ddots & \vdots \\ \delta_1(X^s) & \cdots & \delta_M(X^s) \end{bmatrix} \tag{8}$$

The least-squares method is applied to minimise the error norm to determine the vector of the coefficients.

Several criteria, such as the relative error, the coefficient of determination (R^2) and the root mean squared error ($RMSE$), can be used to evaluate the accuracy of the developed RS model. In this study, there are 25 design points (s=5× 5), and RS models using linear, quadratic, cubic, and quartic polynomials were constructed in sequence. Among the RS models, the quartic model with 15 terms has the best performance.

Fig. 12(a) presents the two quartic RSs constructed under U_{hub}= 6 m/s. For the RS without TMD, R^2=0.996 and $RMSE$=0.068. For the RS with TMD, R^2=0.995 and $RMSE$=0.041. Because of the nonlinear relation between η_{hcr} and H_s and T_p, both RSs are uneven. As anticipated, greater η_{hcr} values appear at lower T_p and higher H_s values. At T_p=4 s, there is a big gap between the two RSs, and this gap tends to shrink gradually as T_p increases. Fig. 12(b) gives an example of the effect of the TMD across T_p. At lower T_p values, the relative reduction in η_{hcr} exceeds 50%. As T_p rises, the influence of TMD decreases, and the relative reduction drops to approximately 40%. Because of limited aerodynamic loads on the monopile system, the hub motions are not affected by the wind speed.

7.2. Relative motions between the blade root and the hub

Eventually, the blade root will be mated with the hub, and the relative motions between them are more critical to the success of the alignment process than the hub motion alone. During the simulations of the present single-blade system, the blade is subjected to drag-type wind loads, and the blade-root motions in the yz-plane are of primary concern. The relative planar motions between the blade root and hub were calculated. As shown in Figs. 13(a)–13(b) under the

selected environmental condition, the relative displacement in the y-direction outweighs that in the z-direction, and the TMD only reduces the range of the y-displacement. The relative motion radius, η_r, was defined in Section 2. When a TMD is used, a reduction slightly higher than 10% is observed in the response maximum (Fig. 13(c)). This reduction is less significant than that of the hub motion alone. The critical relative motion radius, η_{rcr}, can also be obtained by interpolating the η_r-ν relationships for the specified outcrossing rate. When the TMD is applied, η_{rcr} declines from 1.97 m to 1.71 m in this case. Although the reduction is modest for T_p=6 s, it is expected to increase for lower T_p values when stronger resonant responses of the monopile structure are encountered. On the other hand, if T_p is kept the same, but U_{hub} or TI grows, the blade-root motions would play a more important role, and the beneficial effects of the TMD are likely to decrease.

Figs. 14(a)–14(b) present the RSs for η_{rcr} under the two wind conditions. The accuracies of these constructed RSs are comparable to those constructed for the hub motions. As shown in Fig. 14(a), under T_p=4 s and H_s=3 m, the maximum η_{rcr} of the system without the TMD reaches 3.4 m, whereas the η_{rcr} of the system with the TMD decreases to 2.2 m. For higher T_p or lower H_s values, less resonant responses of the monopile structure occur, and the effect of the TMD reduces consequently. A similar trend of variation can be observed in Fig. 14(b). Note that when U_{hub} increases from 6 m/s to 12 m/s, the corresponding RS becomes more uneven because of greater contributions of the blade-root motions to η_{rcr}.

To quantify the impact of TMD, the percentage reduction in η_{rcr} is defined as follows,

$$Percentage\ reduction = \frac{\eta_{rcr,0} - \eta_{rcr,1}}{\eta_{rcr,1}} \times 100\% \tag{9}$$

where the subscript 0 denotes "without TMD" and the subscript 1 denotes "with TMD".

As shown in Fig. 14(c) for U_{hub}=6 m/s, the percentage reduction approaches 30% at T_p=4 s and falls to 10% at T_p=10 s. The percentage reduction varies similarly with regard to H_s or T_p for U_{hub}=12 m/s, but the maximum reduction reduces to 20% at T_p=4 s (Fig. 14(d)). In a sea state suitable for single-blade installation, the effect of the TMD may be modest. However, if waves with short T_p occur during offshore installation, a TMD can be an effective means of reducing η_{rcr}, which is linked to alignment success. Thus, a TMD can be used to expand the weather window of offshore single-blade installation.

8. CONCLUDING REMARKS

This study investigates the impact of a passive tuned mass damper on single-blade installation through multibody simulations. The coupling of the damper system with the HAWC2 program is achieved using an external dynamic link library. The final single-blade installation stage of an assembled monopile system is considered under collinear wind and waves conditions. The conclusions are as follows:

- For the studied OC3 Phase II monopile, an optimised TMD installed at the tower top can substantially increase the damping ratio of the dominant fore-aft mode of the monopile system and can reduce the resonant responses when the monopile structure is subjected to wave loading.

- The effect of the TMD on single-blade installation is evaluated using the hub motion radius and relative motion radius metrics. Response surfaces are constructed to assess the variation in the metrics with regard to significant wave height and spectral peak period. When only the hub motions are considered, the maximum percentage reduction in the critical motion radius due to the TMD can exceed 50% in cases with a small peak period and lower wind speed. When both the blade-root and the hub motions are considered, the maximum percentage reduction in the critical motion radius approaches 30%. For the present installation system, the positive impact of the tuned mass damper decreases under higher wave peak periods and greater wind speeds.

- The influence of the TMD depends on a few factors. On the one hand, the properties of the TMD can be adjusted. The present TMD mass accounts for 1.7% of the structural mass of the assembled monopile without blades. An increase in the TMD mass may amplify the positive impact at the expense of a heavier system. On the other hand, the effect of the TMD is sensitive to the monopile and blade system considered. The studied water depth is 30 m. For similar monopile systems at greater water depths, the effect of the TMD will be greater. In fact, the beneficial effects would also be affected by the lifting equipment in use.

- Detailed design of the TMD is beyond the scope of this study. Although TMDs are a relatively new concept for offshore single-blade installations, previous positive experiences in many civil engineering structures indicate more beneficial effects than the additional cost

of including a TMD [28]. Based on the selected TMD parameters, and if the TMD mass is composed of water, the volume size corresponds to approximately 20 m^3, which is a feasible value [20]. As mentioned above, the TMD is assumed to be mounted at the tower top. During the simulations, the maximum displacement of the TMD from its neutral reference position is close to 1 m, which is smaller than the tower-top radius (1.94 m). End stops may be used in practice for limiting the TMD motions in rougher sea states. The TMD can preferably be pre-installed onshore inside the wind turbine tower and be transported offshore together with the tower. Although the TMD is intended for permanent use after the blade-installation phase, it may be necessary to adjust the damping ratio, considering the increased aerodynamic damping in operational conditions.

9. Acknowledgements

This work has been financially supported by the Research Council of Norway granted through the Department of Marine Technology and the Centre for Research-based Innovation of Marine Operations (SFI MOVE) at NTNU. The author expresses gratitude to Professor Zhen Gao of NTNU for providing the computational resources.

Appendix A. Theoretical Background of a 1-DOF Tuned Mass Damper

The content of this appendix has been adapted from [35]. For simplicity, only brief derivation of the equations is presented. As illustrated in Fig. 4 The TMD is a 1-DOF mass spring damping element acting in the fore-aft (y) direction.

Appendix A.1. Definitions

O : origin point of global inertial reference frame

P : origin point of non-inertial reference frame fixed to the local position where a TMD is at rest

TMD : origin point of a TMD

G : axis orientation of global reference frame

N : axis orientation of local reference frame

$\overrightarrow{r}_{TMD/O_G} = \begin{bmatrix} x & y & z \end{bmatrix}^T_{TMD/O_G}$: position of a TMD with respect to (w.r.t.) O with orientation G

$\overrightarrow{r}_{TMD/P_N} = \begin{bmatrix} x & y & z \end{bmatrix}^T_{TMD/P_N}$: position of a TMD w.r.t. P_N

$\overrightarrow{r}_{TMD_Y}$: position vector for TMD_Y

$\overrightarrow{r}_{P/O_G} = \begin{bmatrix} x & y & z \end{bmatrix}^T_{P/O_G}$: position vector of local position w.r.t. O_G
$R_{N/G}$: 3×3 rotation matrix transforming orientation G to N
$\overrightarrow{\omega}_{N/O_N} = \begin{bmatrix} \dot{\theta} & \dot{\phi} & \dot{\psi} \end{bmatrix}^T_{N/O_N}$: angular velocity of local position in orientation N
$\dot{\overrightarrow{\omega}}_{N/O_N} = \overrightarrow{\alpha}_{N/O_N}$
$\overrightarrow{a}_{G/O_G} = \begin{bmatrix} 0 & 0 & -g \end{bmatrix}^T_{/O_G}$: gravitational acceleration w.r.t. O_N
$\overrightarrow{a}_{G/O_N} = R_{N/G}\,\overrightarrow{a}_{G/O_G} = \begin{bmatrix} a_{G_X} & a_{G_Y} & a_{G_Z} \end{bmatrix}^T_{/O_N}$

Appendix A.2. Equations of Motion

The following relation between the position vectors of the TMD in the reference frame O and of the reference frame P expressed in orientation N holds

$$\overrightarrow{r}_{TMD/O_N} = \overrightarrow{r}_{P/O_N} + \overrightarrow{r}_{TMD/P_N} \tag{A.1}$$

Differentiating twice both sides gives the acceleration of the TMD w.r.t. P oriented with N

$$\begin{aligned} \ddot{\overrightarrow{r}}_{TMD/P_N} = \ddot{\overrightarrow{r}}_{TMD/O_N} - \ddot{\overrightarrow{r}}_{P/O_N} - \overrightarrow{\omega}_{N/O_N} \times (\overrightarrow{\omega}_{N/O_N} \times \overrightarrow{r}_{TMD/P_N}) \\ - \overrightarrow{\alpha}_{N/O_N} \times \overrightarrow{r}_{TMD/P_N} - 2\overrightarrow{\omega}_{N/O_N} \times \dot{\overrightarrow{r}}_{TMD/P_N} \end{aligned} \tag{A.2}$$

Replacing the acceleration in the inertial frame $\ddot{\overrightarrow{r}}_{TMD/O_N}$ with a force balance yields

$$\begin{aligned} \ddot{\overrightarrow{r}}_{TMD/P_N} = \frac{1}{m}\overrightarrow{F}_{TMD/O_N} - \ddot{\overrightarrow{r}}_{P/O_N} - \overrightarrow{\omega}_{N/O_N} \times (\overrightarrow{\omega}_{N/O_N} \times \overrightarrow{r}_{TMD/P_N}) \\ - \overrightarrow{\alpha}_{N/O_N} \times \overrightarrow{r}_{TMD/P_N} - 2\overrightarrow{\omega}_{N/O_N} \times \dot{\overrightarrow{r}}_{TMD/P_N} \end{aligned} \tag{A.3}$$

In Eq. (A.3), the external forces $\overrightarrow{F}_{TMD_Y/O_N}$ are given by

$$\overrightarrow{F}_{TMD_Y/P_N} = \begin{bmatrix} F_{X_{TMD_{Y/ON}}} + m_y a_{G_{X/ON}} \\ -c_y \dot{y}_{TMD_{Y/PN}} - k_y y_{TMD_{Y/PN}} + m_y a_{G_{Y/ON}} \\ F_{Z_{TMD_{Y/ON}}} + m_y a_{G_{Z/ON}} \end{bmatrix} \tag{A.4}$$

Because TMD_Y is fixed to frame N in the x-and z-directions

$$r_{TMD_Y/P_N} = \begin{bmatrix} 0 \\ y_{TMD_{Y/PN}} \\ 0 \end{bmatrix} \tag{A.5}$$

Thus, the other components of Eq. (A.3) are

$$\overrightarrow{\omega}_{N/O_N} \times (\overrightarrow{\omega}_{N/O_N} \times \overrightarrow{r}_{TMD/P_N}) = y_{TMD_{Y/PN}} \begin{bmatrix} \dot{\theta}_{N/ON}\ \dot{\phi}_{N/ON} \\ -(\dot{\theta}^2_{N/ON} + \dot{\psi}^2_{N/ON}) \\ \dot{\phi}_{N/ON}\ \dot{\psi}_{N/ON} \end{bmatrix} \tag{A.6}$$

$$\overrightarrow{\alpha}_{N/O_N} \times \overrightarrow{r}_{TMD_Y/P_N} = y_{TMD_{Y/PN}} \begin{bmatrix} -\ddot{\psi}_{N/ON} \\ 0 \\ \ddot{\theta}_{N/ON} \end{bmatrix} \tag{A.7}$$

$$2\overrightarrow{\omega}_{N/O_N} \times \dot{\overrightarrow{r}}_{TMD_Y/P_N} = 2\dot{y}_{TMD_{Y/PN}} \begin{bmatrix} -\dot{\psi}_{N/ON} \\ 0 \\ \dot{\theta}_{N/ON} \end{bmatrix} \tag{A.8}$$

Therefore, $\ddot{y}_{TMD_Y/P_N}$ is governed by the following equations

$$\ddot{y}_{TMD_Y/P_N} = (\dot{\theta}^2_{N/ON} + \dot{\psi}^2_{N/ON} - \frac{k_y}{m_y}) y_{TMD_Y/P_N} - (\frac{c_y}{m_y}) \dot{y}_{TMD_Y/P_N} - \ddot{y}_{P/O_N} + a_{G_Y/O_N} \tag{A.9}$$

$$\begin{aligned} F_{X_{TMD_{Y/ON}}} = m_y \Big(& - a_{G_X/O_N} + \ddot{x}_{P/ON} - (\ddot{\psi}_{N/ON} - \dot{\theta}_{N/ON}\ \dot{\phi}_{N/ON}) y_{TMD_Y/P_N} \\ & - 2\dot{\psi}_{N/ON}\ \dot{y}_{TMD_Y/P_N} \Big) \end{aligned} \tag{A.10}$$

$$\begin{aligned} F_{Z_{TMD_{Y/ON}}} = m_y \Big(& - a_{G_Z/O_N} + \ddot{z}_{P/ON} + (\ddot{\theta}_{N/ON} + \dot{\phi}_{N/ON}\ \dot{\psi}_{N/ON}) y_{TMD_Y/P_N} \\ & + 2\dot{\theta}_{N/ON}\ \dot{y}_{TMD_Y/P_N} \Big) \end{aligned} \tag{A.11}$$

Appendix A.3. State Equations

Inputs: The inputs are the global linear acceleration and angular position, velocity, and acceleration

$$\overrightarrow{u} = \begin{bmatrix} \ddot{\overrightarrow{r}}_{P/OG} \\ R_{N/G} \\ \overrightarrow{\omega}_{N/O_G} \\ \overrightarrow{\alpha}_{P/O_G} \end{bmatrix} \tag{A.12}$$

States: The position and velocity of the TMD in the local reference frame are

$$\overrightarrow{R}_{TMD/P_N} = \begin{bmatrix} y_{TMD_Y/P_N} \\ \dot{y}_{TMD_Y/P_N} \end{bmatrix} \tag{A.13}$$

The nonlinear first-order equations can be expressed in the state-space form

$$\dot{\overrightarrow{R}}_{TMD} = A\overrightarrow{R}_{TMD} + B \tag{A.14}$$

where

$$A(\overrightarrow{u}) = \begin{bmatrix} 0 & 1 \\ \dot{\theta}^2_{P/O_N} + \dot{\psi}^2_{P/O_N} - \frac{k_y}{m_y} & -(\frac{c_y}{m_y}) \end{bmatrix} \tag{A.15}$$

and

$$B(\overrightarrow{u}) = \begin{bmatrix} 0 \\ -\ddot{y}_{P/O_N} + a_{G_Y/O_N} \end{bmatrix} \tag{A.16}$$

Outputs: The outputs include the reaction forces $\overrightarrow{F}_{PG}$ and moments $\overrightarrow{M}_{PG}$ acting at the node of the tower.

$$\overrightarrow{F}_{PG} = R^T_{N/G} \begin{bmatrix} -F_{X_{TMD_{Y/ON}}} \\ k_y y_{TMD/P_N} + c_y \dot{y}_{TMD_{/PN}} \\ -F_{Z_{TMD_{Y/ON}}} \end{bmatrix} \tag{A.17}$$

$$\overrightarrow{M}_{PG} = R^T_{N/G} \begin{bmatrix} -F_{Z_{TMD_{Y/ON}}} y_{TMD_{/PN}} \\ 0 \\ F_{X_{TMD_{Y/ON}}} y_{TMD_{/PN}} \end{bmatrix} \tag{A.18}$$

References

[1] I. Pineda, P. Tardieu. The European offshore wind industry – key trends and statistics 2016. https://windeurope.org/about-wind/statistics/offshore/european-offshore-wind-industry-key-trends-and-statistics-2016/ Accessed: June 01, 2017.

[2] K. Garus, EEW has produced the world's heaviest monopile, http://www.offshorewindindustry.com/news/eew-produced-worlds-heaviest-monopile, Accessed: July 05, 2017.

[3] H. Veldkamp, J. Van Der Tempel, Influence of wave modelling on the prediction of fatigue for offshore wind turbines, Wind Energy 8 (2005) 49–65.

[4] R. Shirzadeh, C. Devriendt, M. A. Bidakhvidi, P. Guillaume, Experimental and computational damping estimation of an offshore wind turbine on a monopile foundation, Journal of Wind Engineering and Industrial Aerodynamics 120 (2013) 96–106.

[5] M. J. Kaiser, B. Snyder, Offshore wind energy installation and decommissioning cost estimation in the us outer continental shelf, US Bureau of Ocean Energy Management, Enforcement and Regulation (2010).

[6] W. Wang, Y. Bai, Investigation on installation of offshore wind turbines, Journal of Marine Science and Application 9 (2010) 175–180.

[7] M. Gaunaa, L. Bergami, S. Guntur, F. Zahle, First-order aerodynamic and aeroelastic behavior of a single-blade installation setup, Journal of Physics: Conference Series 524 (2014) 012073.

[8] Y. Wang, W. He, D. Tian, Calculation of hoisting forces of the wind turbine rotor based on wind conditions, Renewable Energy 39 (2012) 323–328.

[9] Y. Wang, D. Tian, W. He, Computation of hoisting forces on wind turbine blades using computation fluid dynamics, Applied Mechanics and Materials 446 (2014) 452–457.

[10] M. Gaunaa, J. Heinz, W. Skrzypiński, Toward an engineering model for the aerodynamic forces acting on wind turbine blades in quasisteady standstill and blade installation situations, Journal of Physics: Conference Series 753 (2016) 022007.

[11] L. Kuijken, Single blade installation for large wind turbines in extreme wind conditions, Master of Science Thesis, Technical University of Denmark & TU Delft (2015).

[12] Y. Zhao, Z. Cheng, P.C. Sandvik, Z. Gao, T. Moan. An integrated dynamic analysis method for simulating installation of a single blade for offshore wind turbines. *Under review in Ocean Engineering* (2017).

[13] Liftra ApS. LT575 Blade Dagon. `http://liftra.com/product/blade-dragon/` Accessed: Feb 21, 2017.

[14] High Wind NV. The Boom Lock. `http://www.high-wind.eu/boomlock/` Accessed: Feb 21, 2017.

[15] O. Slettner. Personal communication. January 25, 2017.

[16] Z. Jiang, Z. Gao, Z. Ren, Y. Li, L. Duan, A parametric study on the blade final installation process for monopile wind turbines under rough environmental conditions, Under review in Engineering Structures (2018).

[17] M. Damgaard, L. B. Ibsen, L. V. Andersen, J. K. Andersen, Cross-wind modal properties of offshore wind turbines identified by full scale testing, Journal of Wind Engineering and Industrial Aerodynamics 116 (2013) 94–108.

[18] R. Shirzadeh, W. Weijtjens, P. Guillaume, C. Devriendt, The dynamics of an offshore wind turbine in parked conditions: a comparison between simulations and measurements, Wind Energy 18 (2015) 1685–1702.

[19] B. Spencer Jr, S. Nagarajaiah, State of the art of structural control, Journal of Structural Engineering 129 (2003) 845–856.

[20] M. A. Lackner, M. A. Rotea, Passive structural control of offshore wind turbines, Wind Energy 14 (2011) 373–388.

[21] S. Colwell, B. Basu, Tuned liquid column dampers in offshore wind turbines for structural control, Engineering Structures 31 (2009) 358–368.

[22] A. F. Mensah, L. Dueñas-Osorio, Improved reliability of wind turbine towers with tuned liquid column dampers (TLCDs), Structural Safety 47 (2014) 78–86.

[23] R. Shirzadeh, M. Kühn, Application of two passive strategies on the load mitigation of large offshore wind turbines, Journal of Physics: Conference Series 749 (2016) 012011.

[24] N. Caterino, Semi-active control of a wind turbine via magnetorheological dampers, Journal of Sound and Vibration 345 (2015) 1–17.

[25] J. J. Connor, Introduction to structural motion control, Prentice Hall, 2003.

[26] M. A. Lackner, M. A. Rotea, Structural control of floating wind turbines, Mechatronics 21 (2011) 704–719.

[27] H. Namik, M. Rotea, M. Lackner, Active structural control with actuator dynamics on a floating wind turbine, in: Proceedings of the 51st AIAA Aerospace Sciences Meeting, 2013, pp. 7–10.

[28] G. M. Stewart, M. A. Lackner, The impact of passive tuned mass dampers and wind–wave misalignment on offshore wind turbine loads, Engineering Structures 73 (2014) 54–61.

[29] Y. Si, H. R. Karimi, H. Gao, Modelling and optimization of a passive structural control design for a spar-type floating wind turbine, Engineering Structures 69 (2014) 168–182.

[30] M. L. Brodersen, A.-S. Bjørke, J. Høgsberg, Active tuned mass damper for damping of offshore wind turbine vibrations, Wind Energy 20 (2017) 783–796.

[31] B. Hofmann-Wellenhof, H. Lichtenegger, J. Collins, Global positioning system: theory and practice, Springer Science & Business Media, 2012.

[32] A. M. Hansen, F. Rasmussen, T. J. Larsen, Gearbox loads caused by double contact simulated with hawc2, EWEA Annual Event 2011 (2010).

[33] Z. Jiang, M. Karimirad, T. Moan, Dynamic response analysis of wind turbines under blade pitch system fault, grid loss, and shutdown events, Wind Energy 17 (2014) 1385–1409.

[34] Z. Jiang, L. Yang, Z. Gao, T. Moan, Numerical simulation of a wind turbine with a hydraulic transmission system, Energy Procedia 53 (2014) 44–55.

[35] W. La Cava, M. Lackner, Theory Manual for the Tuned Mass Damper Module in FAST V8, Technical Report, Department of Mechanical and Industrial Engineering, University of Massachusetts Amherst, 2015.

[36] T. J. Larsen, How 2 HAWC2, The User's Manual, Technical Report, Risoe National Laboratory, Technical University of Denmark, Roskilde, 2009.

[37] M. Hansen, Aerodynamics of wind turbines, 2nd ed., Earthscan, London, UK, 2008.

[38] S. F. Hoerner, Fluid-dynamic drag: practical information on aerodynamic drag and hydrodynamic resistance, Hoerner Fluid Dynamics Midland Park, NJ, USA, 1965.

[39] O. Faltinsen, Sea loads on ships and offshore structures, Cambridge University Press, 1993.

[40] D. C. Montgomery, Design and analysis of experiments, John Wiley & Sons, 2017.

[41] Z. Jiang, M. Gu, Optimization of a fender structure for the crashworthiness design, Materials & Design 31 (2010) 1085–1095.

[42] H. Fang, M. Rais-Rohani, Z. Liu, M. Horstemeyer, A comparative study of metamodeling methods for multiobjective crashworthiness optimization, Computers & Structures 83 (2005) 2121–2136.

[43] G. G. Wang, S. Shan, Review of metamodeling techniques in support of engineering design optimization, Journal of Mechanical Design 129 (2007) 370–380.

[44] J. Jonkman, W. Musial, Offshore Code Comparison Collaboration (OC3) for IEA Task 23 Offshore Wind Technology and Deployment Technical Report NREL/TP-5000-48191, Technical Report, National Renewable Energy Laboratory, Golden, CO, USA, 2010.

[45] P. Passon, Memorandum: derivation and description of the soil-pile-interaction models, IEA-Annex XXIIII Subtask 2 (2006).

[46] L. Li, Z. Gao, T. Moan, Joint distribution of environmental condition at five european offshore sites for design of combined wind and wave energy devices, Journal of Offshore Mechanics and Arctic Engineering 137 (2015) 031901.

[47] International Electrotechnical Comission, IEC 614001 Wind Turbine Part 1: Design Requirements. 3rd ed. edn., Geneva, Switzerland, 2007.

[48] K. Hasselmann, Measurements of wind wave growth and swell decay during the joint north sea wave project (jonswap), Deutschen Hydrografischen Zeitschrift 8 (1973) 95.

[49] R. H. Myers, D. C. Montgomery, C. M. Anderson-Cook, Response surface methodology: process and product optimization using designed experiments, 3rd ed., volume 705, John Wiley & Sons, Inc., Hoboken, New Jersey, USA, 2009.

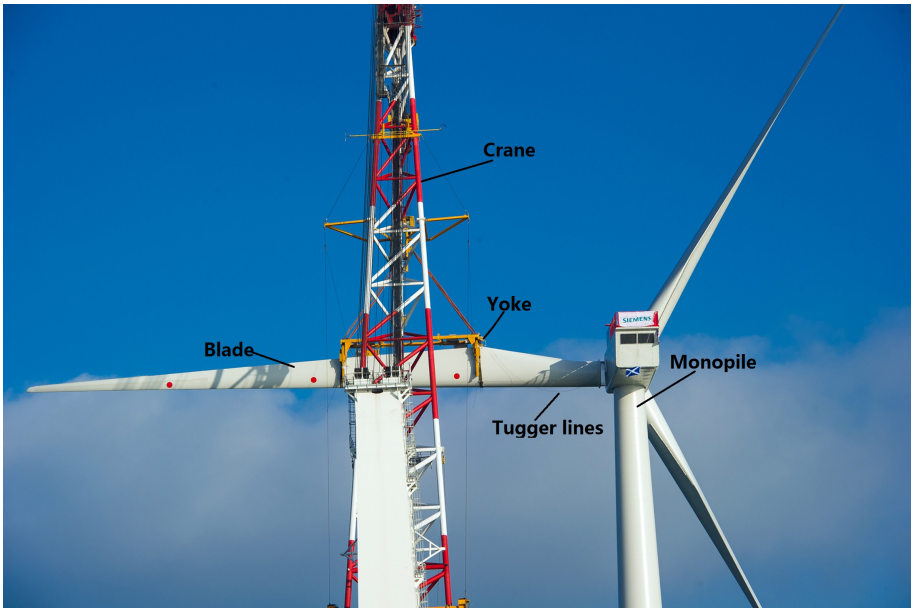

(a)

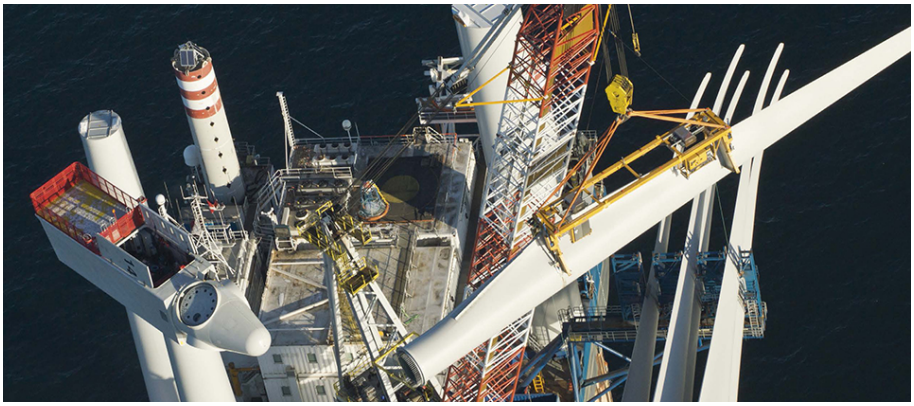

(b)

Figure 1: Image of a horizontal single blade mounting on offshore wind turbines (a) side view (Image source: Siemens Wind Power GmbH) (b) top view (Image source: A2SEA A/S)

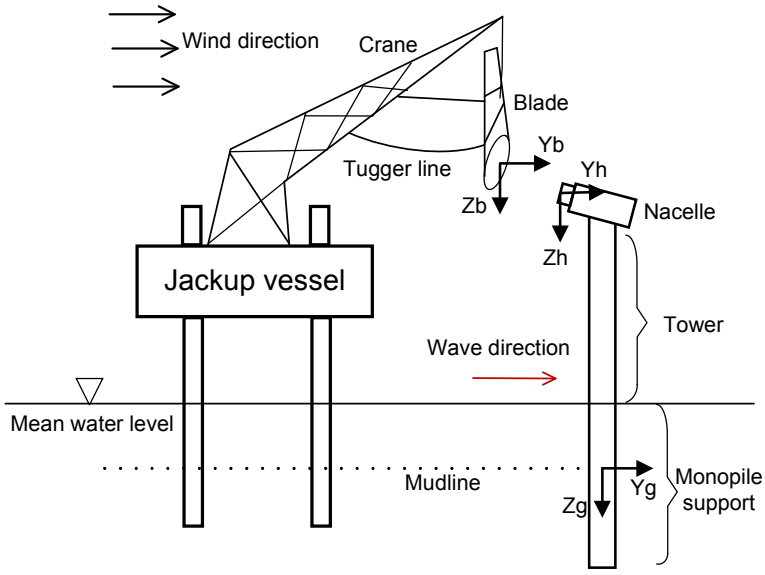

(a)

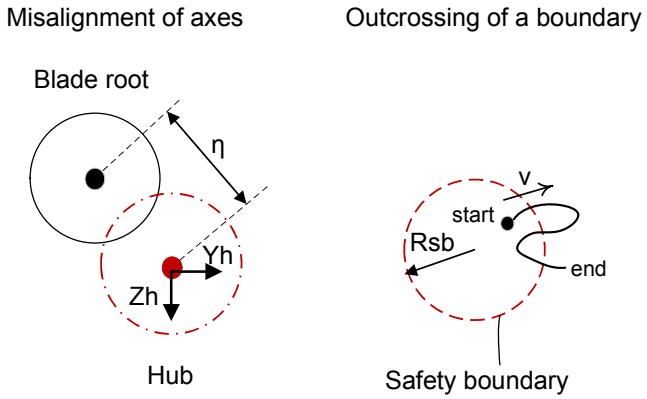

(b)

Figure 2: (a) Schematic of the single blade alignment scenario for a monopile wind turbine (b) relative positions of the blade root and the hub in the yz-plane

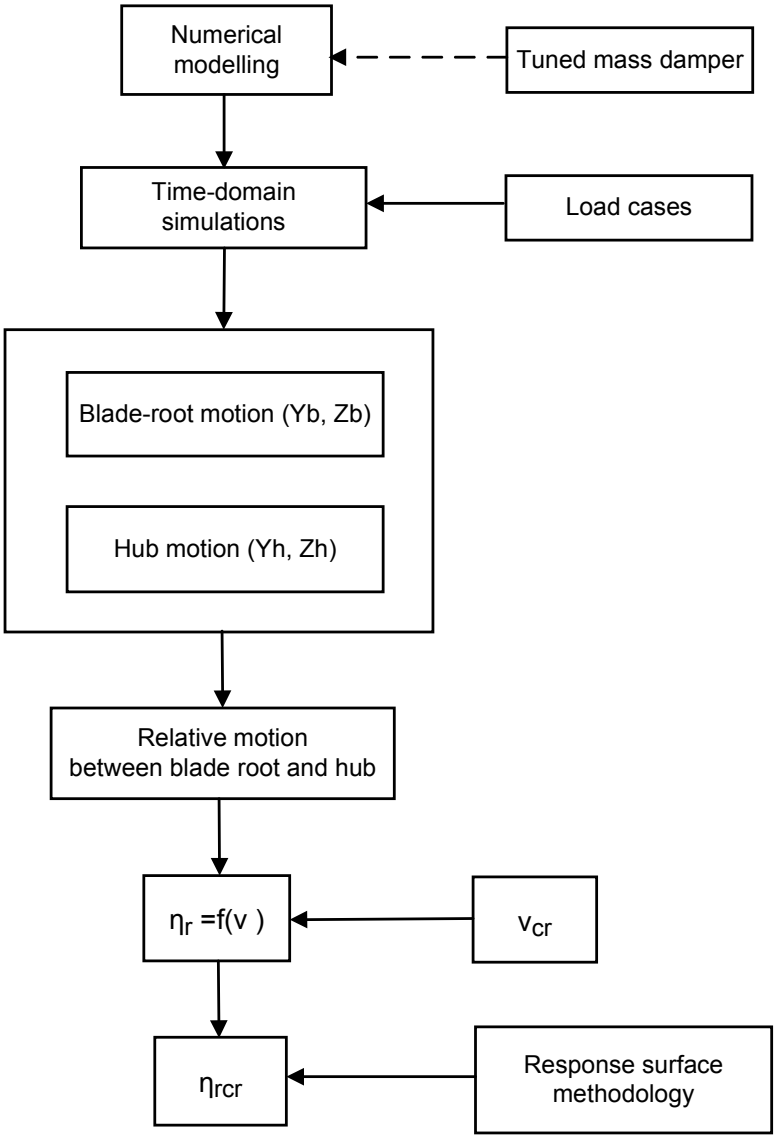

Figure 3: Analysis flowchart of the present paper

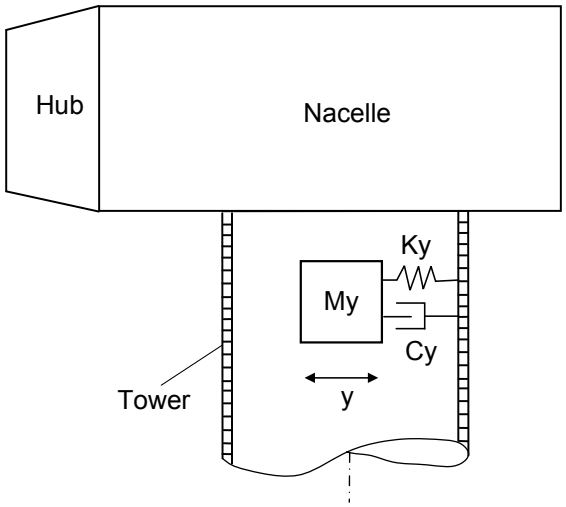

Figure 4: Schematic of a TMD inside the tower structure

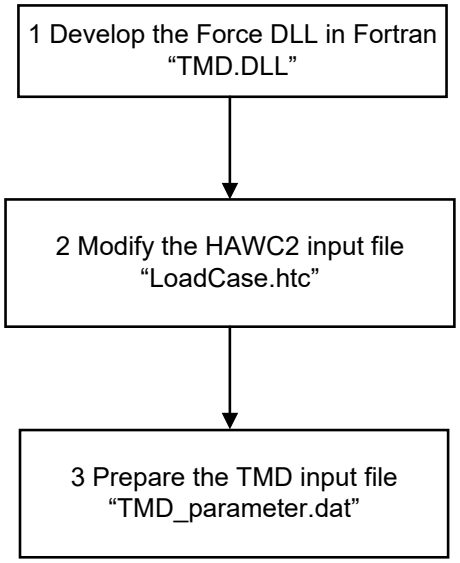

Figure 5: Procedure for modelling a TMD in HAWC2

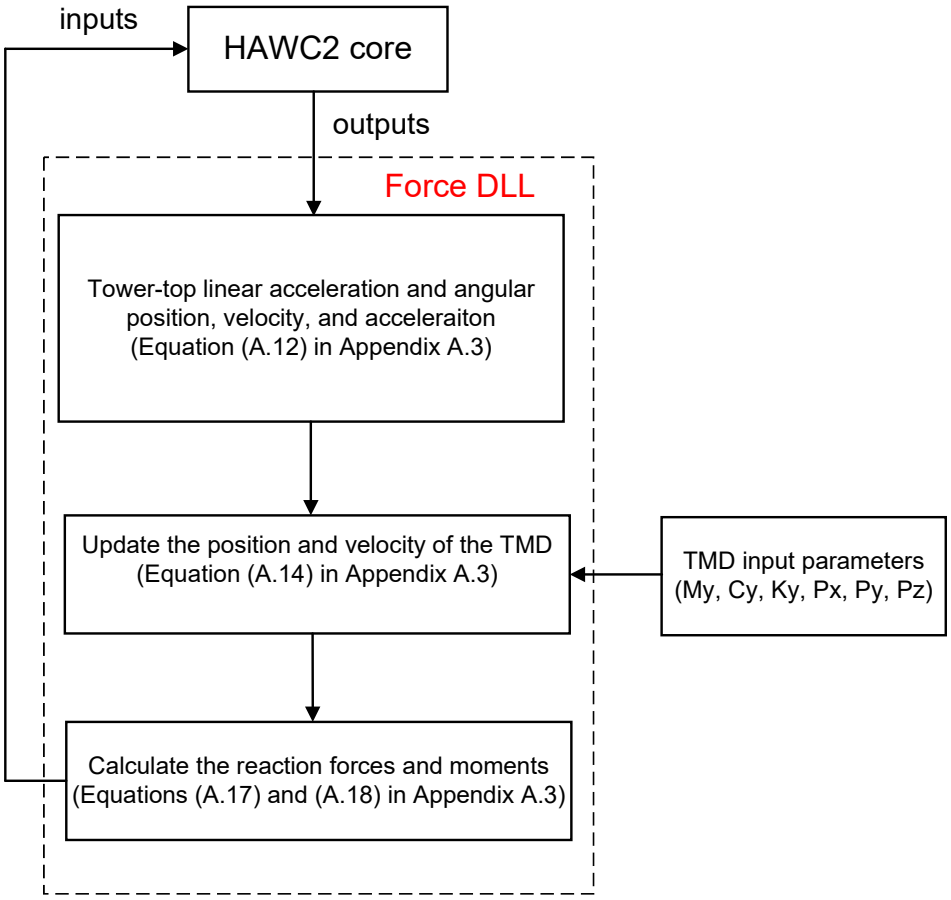

Figure 6: Computational procedure of the TMD module

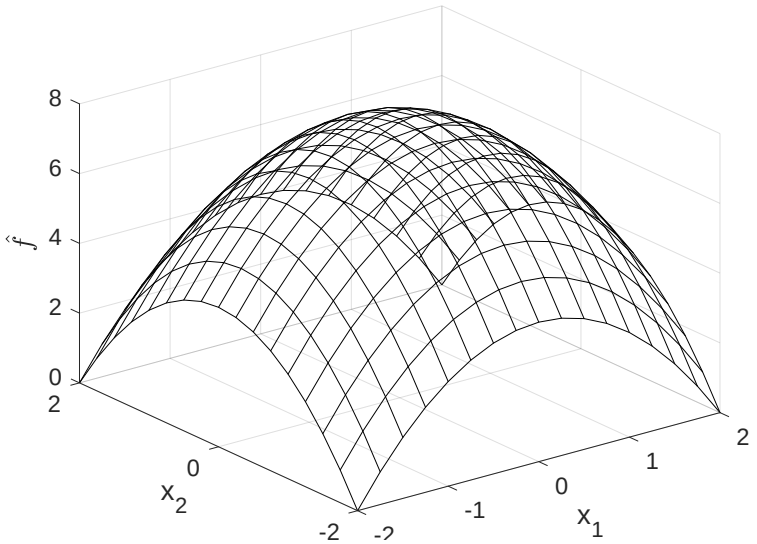

Figure 7: A three-dimensional response showing the expected response as a function of two variables

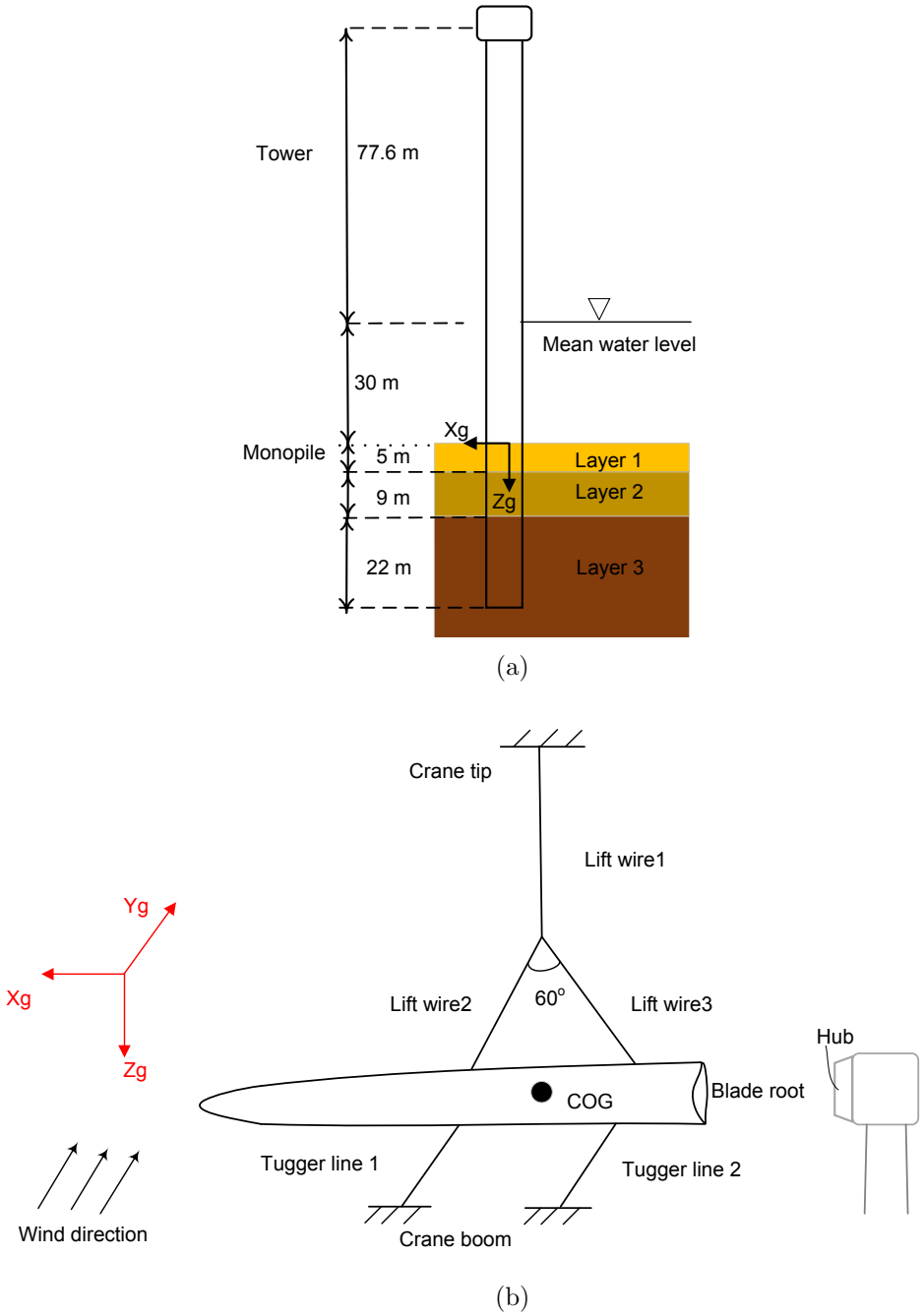

Figure 8: Schematic of the numerical models (a) assembled monopile system (b) single-blade system

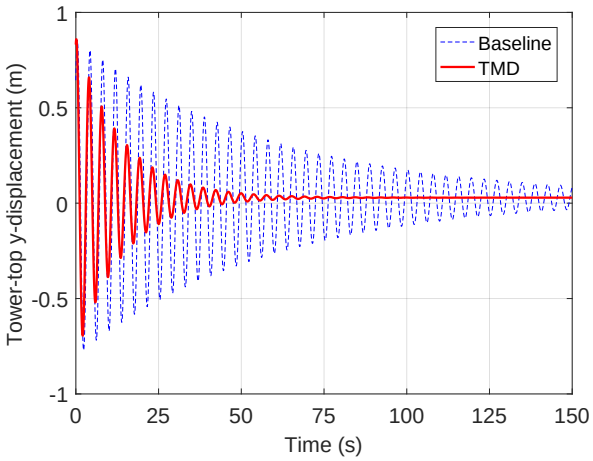

(a)

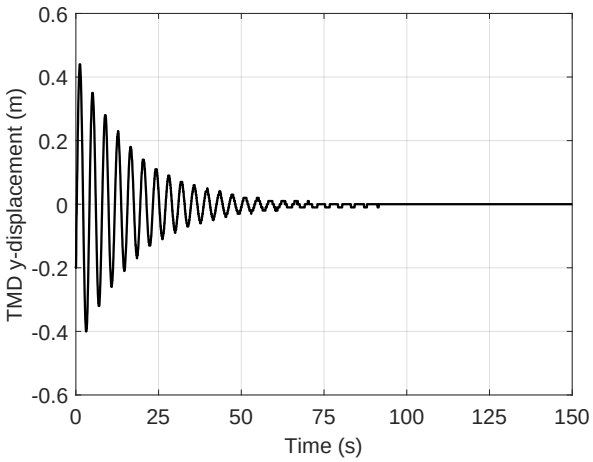

(b)

Figure 9: Decay test of the assembled monopile system: (a) time series of the tower-top displacement in the y-direction (b) displacement of the TMD in the y-direction

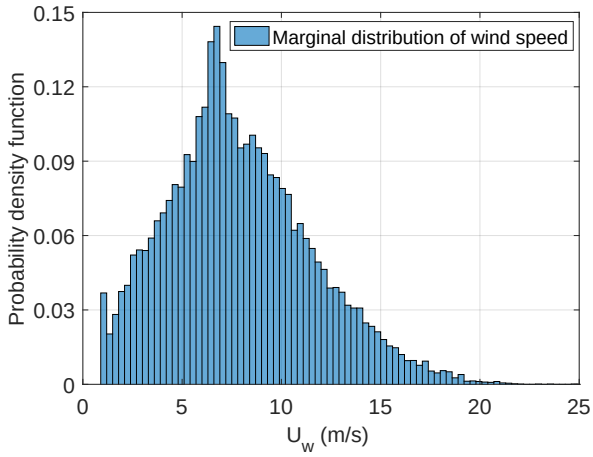

(a)

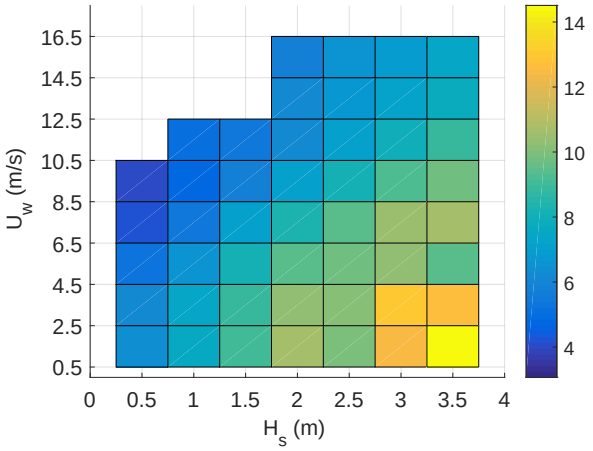

(b)

Figure 10: Hindcast data of the "North Sea Center" site (a) marginal distribution of mean wind speed at 10-m height (b) mean value of T_p for each wind-wave class

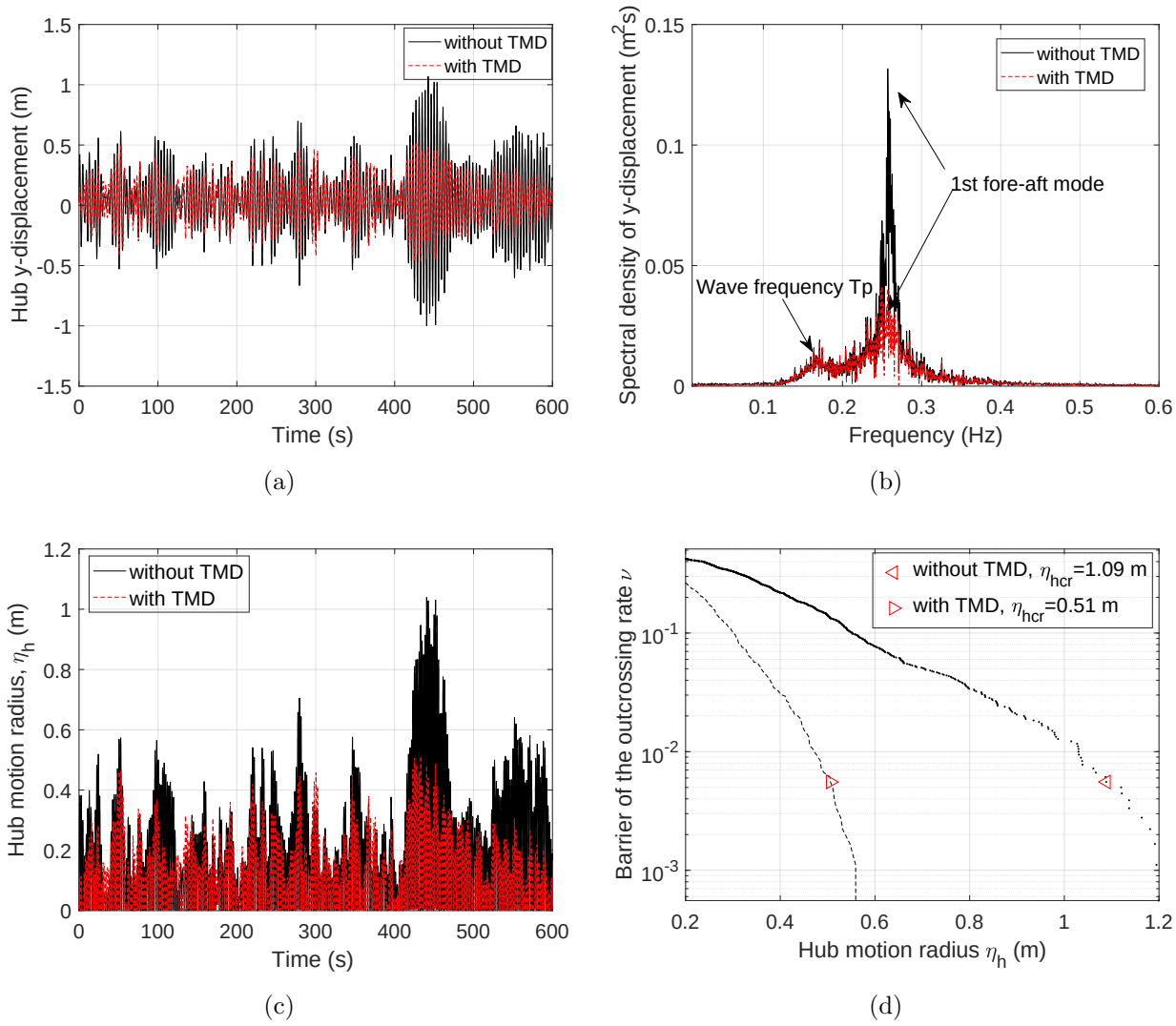

Figure 11: Results of U_{hub}=6 m/s, H_s=2.5 m, T_p=6 s, seed 1 (a) time series of the hub displacement in the fore-aft direction (b) spectra of the hub y-displacement (c) time series of the hub motion radius, η_h (d) variation of the outcrossing rate with the hub motion radius (ν_{cr}=$5.5 \cdot 10^{-3}$ Hz)

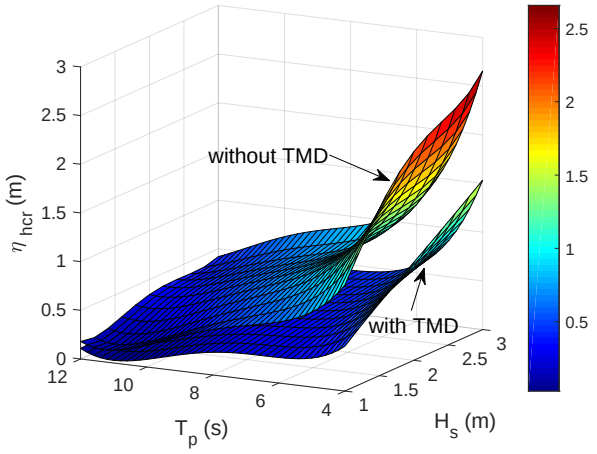

(a)

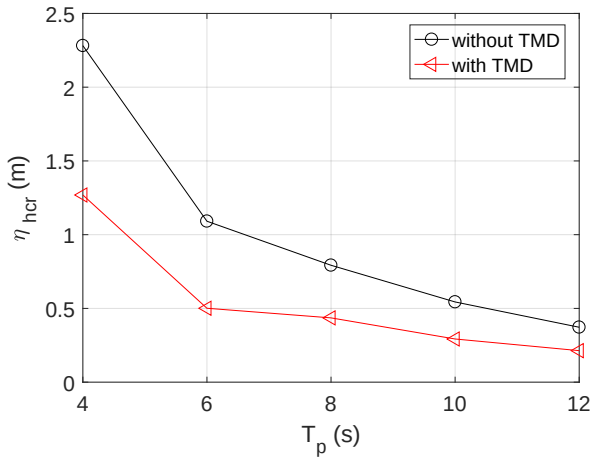

(b)

Figure 12: Results of η_{hcr} under U_{hub}=6 m/s (a) quartic response surface, U_{hub}=6 m/s (b) variation of η_{hcr} with T_p, H_s=2.5 m

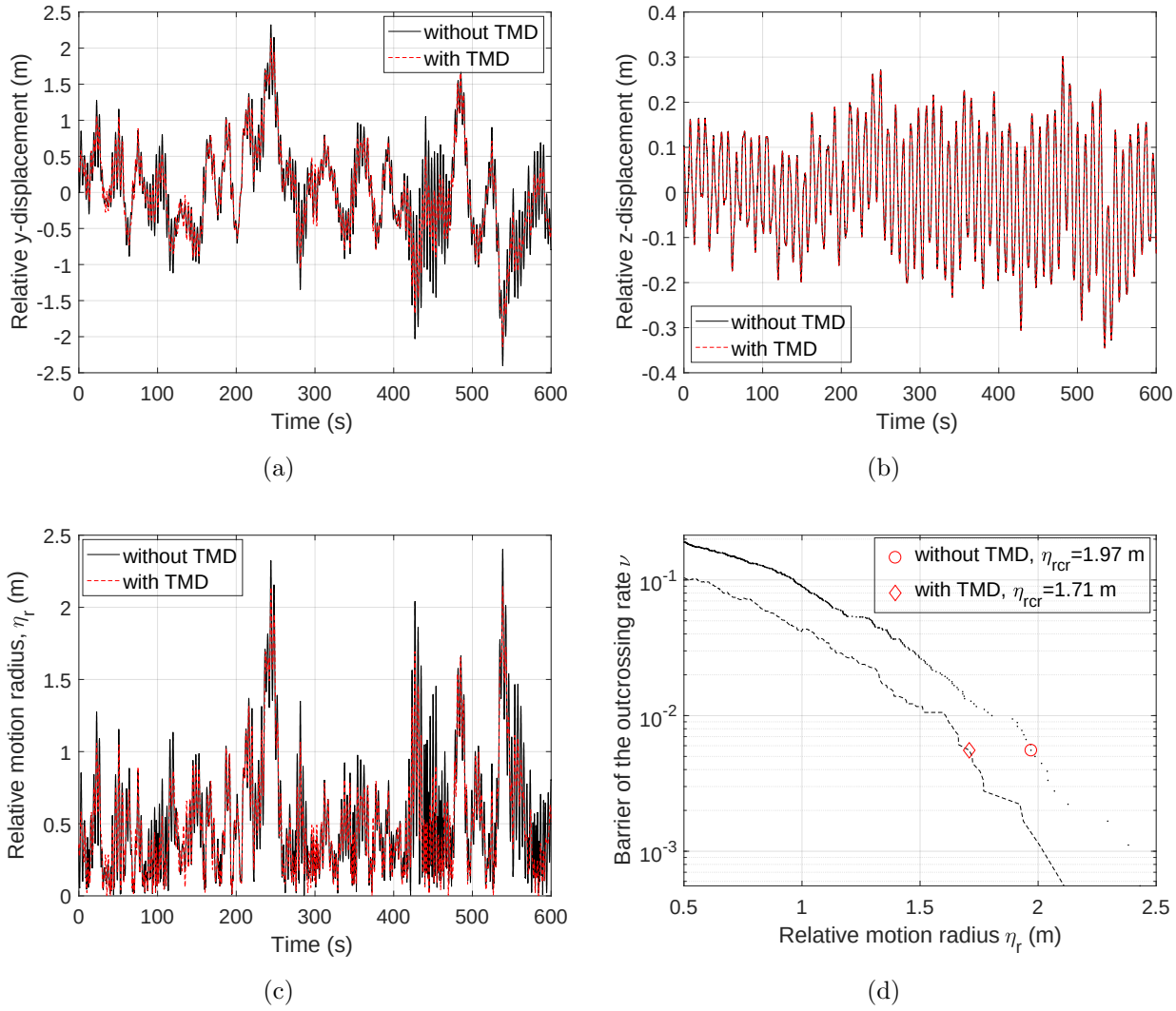

Figure 13: Results of H_s=2.5 m, T_p=6 s, U_{hub}=6 m/s, seed 1 (a) time series of the relative y-displacement (b) time series of the relative z-displacement (c) time series of the relative motion radius in the yz-plane (d) variation of the outcrossing rate ν with the relative motion radius η_r, ν_{cr}=$5.5 \cdot 10^{-3}$

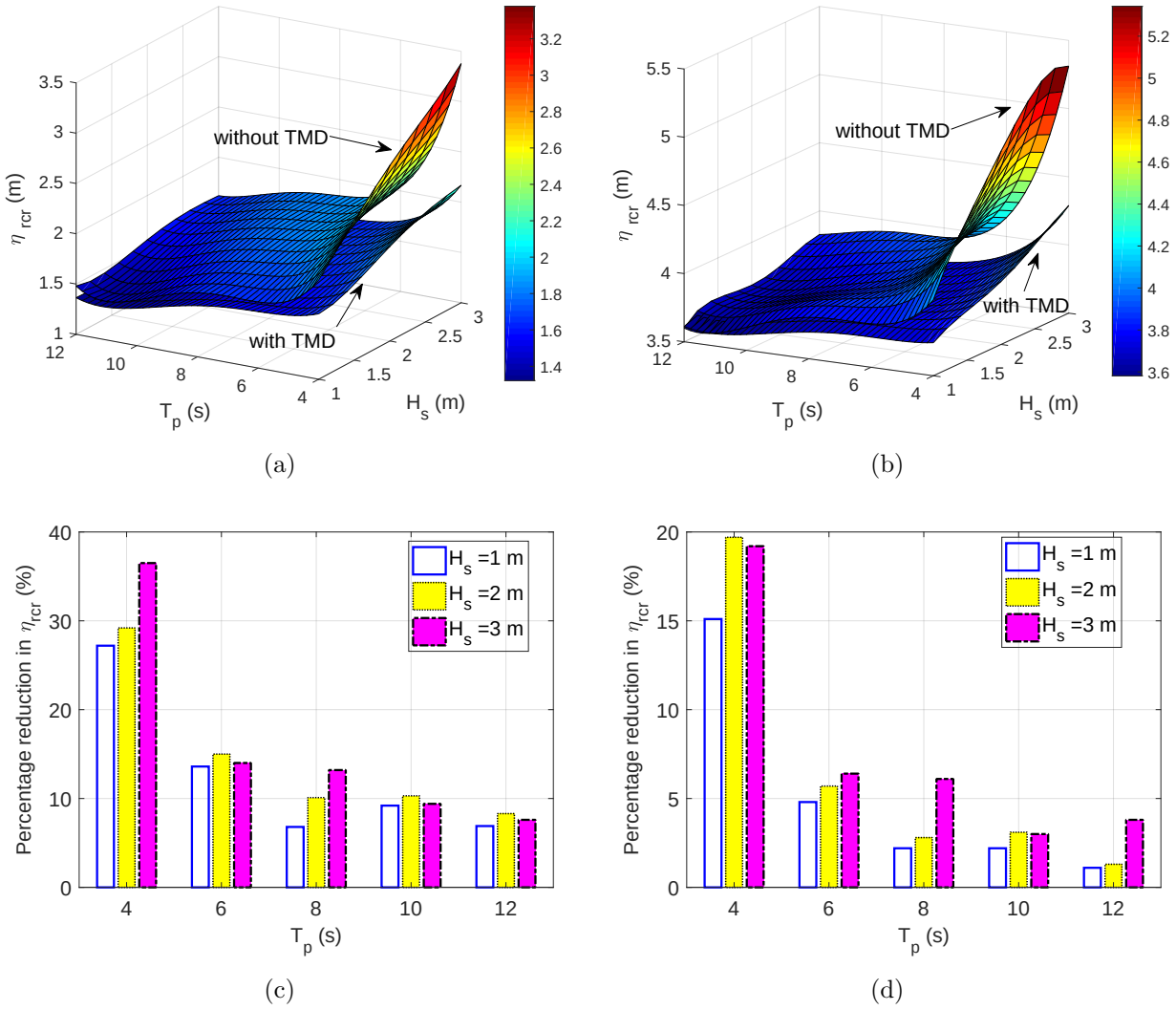

Figure 14: Results of η_{rcr} (a) quartic response surface, U_{hub}=6 m/s (b) quartic response surface, U_{hub}=12 m/s (c) percentage reduction due to TMD, U_{hub}=6 m/s (d) percentage reduction due to TMD, U_{hub}=12 m/s